Scientific Research Publishing

Regulating Electron-Hole Separation to Promote the Photocatalytic Property of BiOBr$_{1-x}$I$_x$/BiOBr Local Distorted Hierarchical Microspheres

Rui Cheng, Yan Zhang*, Yanhua Peng, Xiaolong Yang, Jianqiang Yu, Zhaoguang Nie*

School of Chemistry and Chemical Engineering, Qingdao University, Qingdao, China
Email: *zhangyanchem@qdu.edu.cn, *nzgqdu@163.com

Abstract

In this work, hierarchical BiOBr$_{1-x}$I$_x$/BiOBr heterojunction photocatalyst with a microsphere morphology was synthesized by a facile solvothermal process. It demonstrated that the local structure of the photocatalysts was highly distorted due to the substitution of bromide ions by iodine ions. The photocatalytic properties were evaluated by the photodecomposition of aqueous phenol solution under visible-light irradiation. The results indicated that all the composite photocatalysts exhibited high photocatalytic activity. In particularly, the BiOBr$_{1-x}$I$_x$/BiOBr (x = 0.25) sample exhibited over 92% degradation efficiency of phenol within 150 min, which is 24.6 and 3.08 fold enhancement in the photocatalytic activity over the pure phased BiOBr and BiOI, respectively. Moreover, this excellent photocatalytic property can be expanded to other colorless organic contaminants, verifying the common applicability of BiOBr$_{1-x}$I$_x$/BiOBr (x = 0.25) as an excellent visible-light photocatalyst for organics decomposition. The significant improvement in the photocatalytic activity can be explained by the high efficiency of charge separation due to the enhancement in the internal electric fields and band match that comes from the local structure distortion. This work provides valuable information for the design of highly active photocatalysts toward the environmental remediation.

1. Introduction

Semiconductor photocatalysis has attracted tremendous interest as a green and efficient technique to carry out the degradation of organic pollutants [1] [2]. During the typical photocatalytic process, the low efficiency of carriers (*i.e.*, electron and hole pairs) separation is one of the key factors limiting the activity of photocatalytic materials [3]. On account of the limitation of the carriers' separation, even photocatalyst with a broad spectrum of light absorption cannot exhibit a high photocatalytic activity [4]. The enhancement of the built-in electric field in semiconductors has been found to have a great effect on the improvement of carriers separation [5] [6] and the transport efficiency. Accordingly, various strategies, such as hetero/homojunction [7] [8], elemental doping [9] [10], crystal facet engineering [11] [12], and so on, have been employed to enhance the built-in electric field.

In recent years, various lamellar bismuth based compounds, *e.g.* BiO_X (X = Br, I, Cl) [7], $BiOIO_3$ [13], $Bi_2O_2(OH)(NO_3)$ [14], Bi-M-O (M = V, Mo, W) [15] [16], and so on, have been synthesized and gradually developed to be a series of materials that widely applied in the field of photocatalysis [17]. Compared to the conventional semiconductor photocatalysts, these series of layered bismuth-based materials not only support the forming of an internal electric field to allow the charges diffusion between layers, but also provide abundant distance to polarize orbitals and atoms, enabling the electron-hole pairs separate efficiently [11]. Jiang *et al.* demonstrated that on single-crystal BiOCl nanosheets, the intensity of the internal electric field was dependent on the exposing ratio of the {001} facet, in which BiOCl nanosheets with more exposed {001} facets exhibited higher activity for photocatalytic pollutant degradation under UV light [12]. Sun and co-workers constructed a heterostructure of BiOI(001)/Bi- OCl(010). They demonstrated that beyond achievement of lattice and band match, the shorter photogenerated electron diffusion distance in the self-in- duced internal electric fields of BiOCl slabs leads to a higher charge injection of BiOI(001)/BiOCl(010) [7]. These observations indicate that the crystal facet combination playsa key factorfor enhancing the photocatalytic. Zhang *et al.* reported that incorporating carbon into the Bi_3O_4Cl lattice could increase internal electric field (IEF), and strong IEF could separate electrons and holes effectively, and confine them within $[Bi_3O_4]$ and [Cl] slices to restrict their recombination during their migration from the bulk to the surface [9]. Ren and co-workers synthesized the fluorine isomorphously substituted $BiOBr_xI_{1-x}$ solid solution with various OVs concentrations, and assumed that the excellent photocatalytic performance was due to the synergistic effect of IEF and OVs by fluorine substitution, which could change the charge distribution and promote the separation of photogenerated carriers [10]. Many efforts have been done in tuning IEF or polarizing the related atoms and orbitals, but it still remains unclear to address the key issue of IEF tuning for the photocatalysts with layered structure.

In this work, a series of $BiOBr_{1-x}I_x$/BiOBr hierarchical microsphere photoca-

talyst were designed and controllably synthesized by a conventional solvothermal process. The visible-light photocatalytic activity was evaluated by the degradation of phenol, which was selected as a colorless probe organic contaminant. An enhanced efficiency of photocatalytic phenol degradation under visible light has been achieved over the optimal $BiOBr_{1-x}I_x/BiOBr$ (x = 0.25) sample. It elucidated that the local distortion increases due to elemental doping and heterojunction construction resulted in the spontaneous polarization enhancement and therefore the variation in the built-in electrical field. It is believed that the design of such layered materials could bring a new common strategy to create advance photocatalytic materials for environmental remediation.

2. Experimental Section

2.1. Materials

All chemical reagents used in this work were analytical reagent grade and without further purification. Bismuth nitrate pentahydrate ($Bi(NO_3)_3 \cdot 5H_2O$), potassium bromide (KBr), potassium iodide (KI), ethylene glycol (EG, $C_2H_6O_2$), phenol, bisphenol A (BPA), 2,4-Dichlorophenol (2,4-DCP), sodium sulphate (Na_2SO_4), acetylacetone ($C_5H_8O_2$) and Triton X-100 were purchased from Sinopharm Chemical Reagent Co. Ltd. Deionized water was used throughout the experiments.

2.2. Catalysts Preparation

The photocatalysts were synthesized through a facile solvothermal method. Firstly,the amount of KBr and KI were calculated with different molar Br:I ratios of 2:0, 1.5:0.5, 1:1, 0.5:1.5 and 0:2. In a typical procedure, 2.425 g $Bi(NO_3)_3 \cdot 5H_2O$ and a certain amount of KBr were dissolved in 20 mL and 10 mL of EG solution under ultrasonication at room temperature, respectively. Then, the KBr solution was added to the $Bi(NO_3)_3$ solution under continuous stirring for 30 min. 10 mL of an ethylene glycol (EG) solution containing a certain amount of KI was added dropwise and stirred for another 30 min. Then the resulting mixture was transferred to a 100 mL Teflon-coated autoclave and kept at 100°C for 8 h. After being cooled to room temperature, the precipitates formed were collected through centrifugation and washed with water and ethanol for three times, respectively. The products were then dried at 60°C for 6 h. The obtained powder was denoted as $BiOBr$, $BiOBr_{1-x}I_x/BiOBr$ (x = 0.25), $BiOBr_{1-x}I_x/BiOBr$ (x = 0.5), $BiOBr_{1-x}I_x/BiOBr$ (x = 0.75) and $BiOI$, respectively.

2.3. Characterization

To identify the material composition and the crystal phase of the synthesized samples, XRD patterns were collected by using a Bruker D8 X-ray diffractometer with Cu K_α radiation (λ = 0.15418 nm). The scanning electron microscope (SEM) characterizations were performed on JSM-6700 F field emission scanning electron microscope. The energy dispersive spectrometer (EDS) images were

used to analysis elemental composition of the samples. Transmission electron microscopy (TEM) and High-resolution transmission electron microscopy (HRTEM) were performed on a JEOL JEM-2100 microscope at an acceleration voltage of 200 kV. XPS studies were carried out at a ESCALAB250 electronic spectrometer (Thermo, US) using an Al K_α excitation source (hv = 1486.6 eV). The position of the C 1s peak was taken as a standard (with a banding energy of 284.8 eV). Radicals detection experiments were examined by JES-FA200 electron spin-paramagnetic resonance (ESR) instrument (JEOL). The Brunauere-Emmette-Teller (BET) surface areas of the samples were measured by a N_2 sorption analyzer (BEISHIDE INSTRUMENT CORP, 3H-2000PM2) at a liquid nitrogen temperature. The UV-Vis spectra were recorded on a Hitachi U-41000 spectrophotometer.

2.4. Photocatalytic Activity

The visible-light-driven photocatalytic performances of the samples were estimated by measuring the degradation of phenol (10 mg/L). A 300W Xe lamp (Perfect Light, PLS-SXE300) equipped with a 420 nm cut-off filter provided visible-light irradiation. 50 mg of catalysts was dispersed into 50 ml aqueous solution containing the pollutants. The suspension was stirred in the darkness for 60 min to accomplish absorption-desorption equilibrium. After illumination, 4 ml solution was collected at some time intervals and centrifuged to remove the powder. The absorption spectrum and absorption peak of centrifuged solution were analyzed using a UV-vis spectrometer (Shimadzu 3600PLUS).

To investigate the universal applicability of $BiOBr_{1-x}I_x/BiOBr$ (x = 0.25) sample, several industrial contaminants (BPA (10 mg/L) and 2,4-DCP (10 mg/L)) were also degraded in the similar condition of phenol, and their concentrations were also analyzed by UV-vis spectrometer. The mineralization of phenol, BPA and 2,4-DCP in aqueous solution was analyzed using total organic carbon (TOC) analyzer (Shimadzu TOC-L-CPN).

2.5. Photoelectrochemical Measurement

The transient photo-current measurements and electrochemical impedance spectroscopy (EIS) were recorded in a three-electrode quartz cell by using an Electrochemical Workstation (B.V Vertex. C. EIS, Ivium Technologies, Netherlands). The 0.5 M Na_2SO_4 aqueous solution was used as the electrolyte. The fabricated photoanodes, a Pt foil, and Ag/AgCl electrode were used as working, counter and reference electrode, respectively. The working electrodes were prepared by doctor blade method. A mixture of 20 mg photocatalyst powder, 40 μLdeionized water and a certain ratio of acetylacetone and triton X-100 was coated on a 1 cm × 2 cm FTO glass, followed by annealing at 200˚C for 120 min in atmosphere. A short-arc xenon lamp (Perkin-Elmer, PE300BF) with a cutoff filter ($\lambda \geq 420$ nm) was used as the visible-light source.

3. Results and Discussion

3.1. Morphology and Structure of the Hierarchical Microsphere

X-ray powder diffraction (XRD) was carried out to investigate the crystal phase of the as-prepared samples [18]. **Figure 1** shows the crystalline structures of the synthesized samples. It can be seen from pure BiOBr that characteristic diffraction peaks detected at 10.90˚, 25.21˚, 31.72˚, 32.27˚, 46.28˚ and 57.20˚ were clearly observed. There characteristic diffraction peaks can be attributed to the (001), (101), (102), (110), (200) and (212) crystal planes of tetragonal phase of BiOBr (PDF#09-0393), respectively [19]. While for pure BiOI, strong diffraction peaks, which can be identified at 29.74˚, 31.73˚, 45.49˚ and 55.30˚, and ascribed to the (012), (110), (020) and (122) planes of the tetragonal BiOI (PDF#73-2062), respectively [20]. Characteristic peaks of both BiOBr and BiOI were clearly identified in the $BiOBr_{1−x}I_x/BiOBr$ composites. Remarkably, as shown in the enlarged XRD patterns (**Figure 1(b)**), when the iodine was introduced in the microspheres structures, the diffraction peaks significantly shift toward lower angles, resulting from the larger radius of $I^−$ with respect to $Br^−$ [21]. These results indicate that part of bromide atoms had been replaced by the iodine atoms in the lattice and the series of $BiOBr_{1−x}I_x/BiOBr$ composites had been successfully synthesized.

Figure 2 shows the morphologies and element analysis of pure BiOBr, pure BiOI and $BiOBr_{1−x}I_x/BiOBr$ (x = 0.25) composite. It can be clearly observed from SEM image (**Figures 2(a)-(c)**) that all samples showd a flower-like morphology, which were composed of nanosheets with a thickness of about 10 - 20 nm. The diameters of microspheres are about 3 μm, and these nanosheets contained many gaps which were in favor for the interfacial charge transfer [22]. It is interesting that the nanosheets of iodine doped composite $BiOBr_{1−x}I_x/BiOBr$ (x = 0.25) are rather thinner and more unconsolidated than that of pure BiOBr. To further illustrate the distribution of $BiOBr_{1−x}I_x/BiOBr$ (x = 0.25), energy dispersive spectroscopy (EDS) elemental mapping was performed and the results were
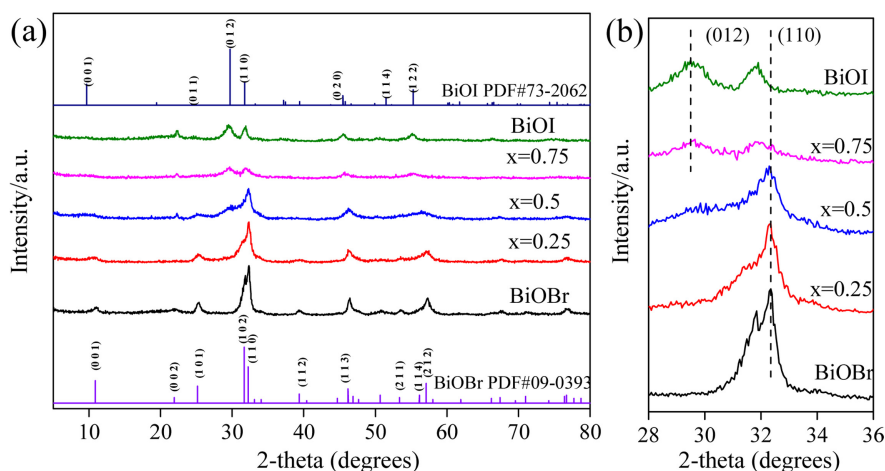

Figure 1. XRD patterns of the as-prepared samples: (a) 5˚ - 80˚ and (b) 28˚ - 34˚.
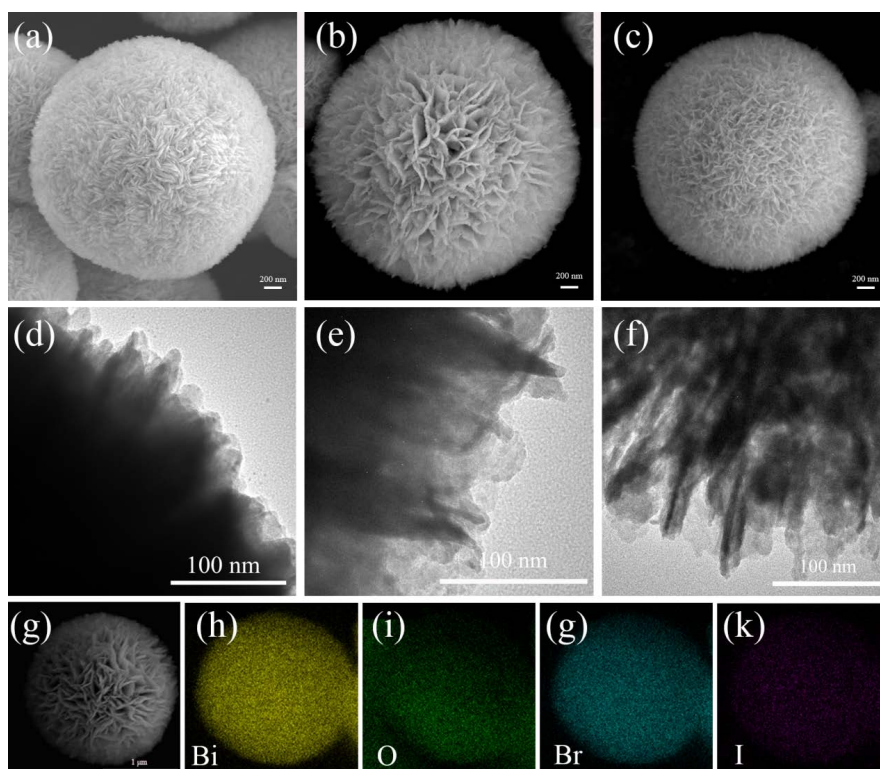
Figure 2. SEM and TEM images of pure BiOBr ((a), (d)), BiOBr$_{1-x}$I$_x$/BiOBr (x = 0.25) ((b), (e)) and pure BiOI ((c), (f)), and EDS elemental mapping images of BiOBr$_{1-x}$I$_x$/BiOBr (x = 0.25) ((g)-(k)).

shown in **Figures 2(g)-(k)**. The elements of Bi, O, Br and I all can be obviously seen and their distributions are highly homogeneous on the surface of BiOBr$_{1-x}$I$_x$/BiOBr (x = 0.25) microspheres.

From the corresponding HRTEM image (**Figure 3**), good crystalline structure and clear lattice fringes can be observed. The interplanar d-spacing of about 0.279 nm and 0.299 nm in **Figure 3(a)** and **Figure 3(c)** could be ascribed to the (110) lattice plane of BiOBr and BiOI nanosheets, respectively [23]. As shown in **Figure 3(b)**, the fringes with the lattice spacing of 0.285 nm matched well with the (110) lattice plane of BiOBr$_{1-x}$I$_x$, and the lattice spacing of 0.279 nm in the outer layer was assigned to the (110) facet of BiOBr [24]. The SAED patterns in the inset picture of **Figure 3(b)** illustrated that a polycrystalline structure has been fabricated. The above results suggested the heterojunction structures with intimate interface contact between BiOBr$_{1-x}$I$_x$ and BiOBr had been formed. This heterojunction structure is beneficial for the electron transfer process during photocatalytic processes [7].

To measure the chemical composition of as-prepared photocatalysts, X-ray photoelectron spectroscopy (XPS) measurement was performed to determine the exact surface state [25]. As shown in **Figure 4(a)**, the survey scan spectra listed the peaks of Bi 4f, O 1s, Br 3d and/or I 3d elements which were calibrated by the C 1s at a binding energy of 284.8 eV [23]. This indicates the high purity of these samples except the slight adventitious hydrocarbons [20]. As shown in
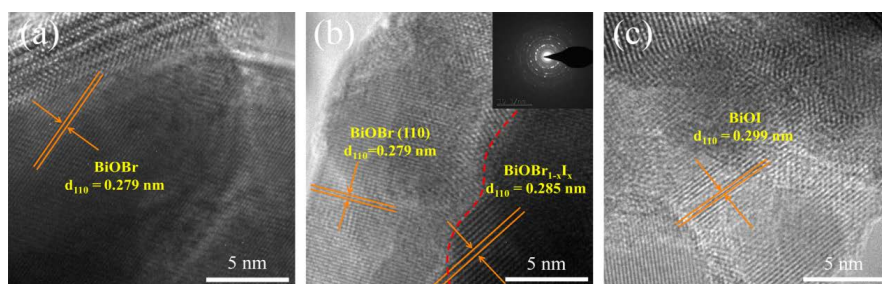
Figure 3. HRTEM images of pure BiOBr (a), BiOBr$_{1-x}$I$_x$/BiOBr (x = 0.25) (x = 0.25) (b) and pure BiOI (c).

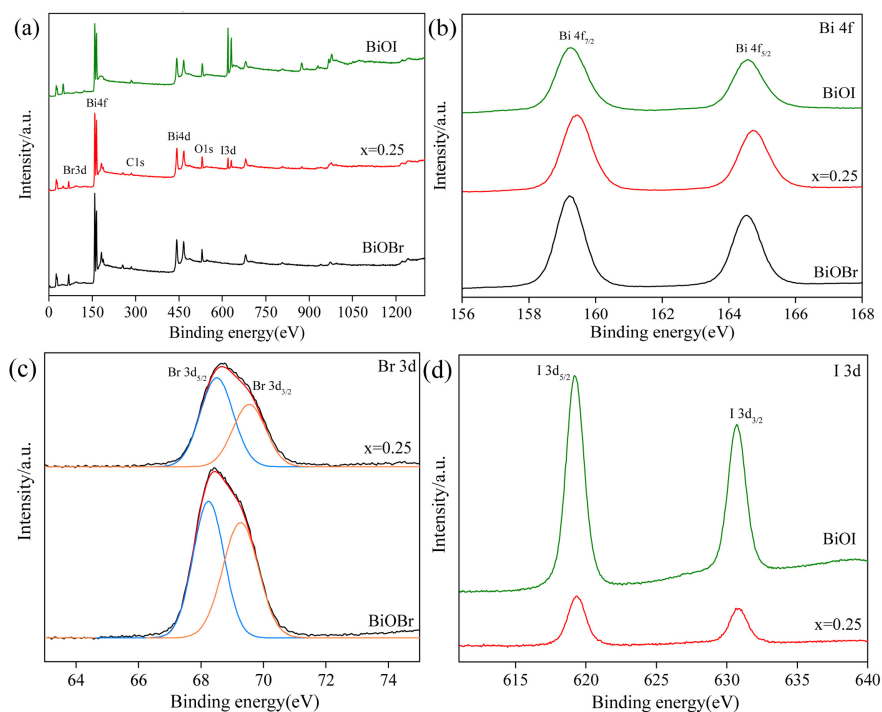**Figure 4.** XPS spectra of pure BiOBr, BiOBr$_{1-x}$I$_x$/BiOBr (x = 0.25) and pure BiOI: (a) survey; (b) Bi 4f spectrum; (c) Br 3d spectrum; and (d) I 3d spectrum.

Figure 4(b), the binding energy to Bi 4f$_{7/2}$ peak at 159.2 eV and Bi 4f$_{5/2}$ peak at 164.5 eV were detected, which demonstrated that Bi existed in the form of Bi^{3+} [26] [27]. Two typical peaks were observed in Br 3d spectra at 68.2 and 69.3 eV (**Figure 4(c)**), which can be assigned to Br 3d$_{5/2}$ and Br 3d$_{3/2}$ in the composites, respectively [28]. That can be confirmed that the presence of Br$^-$. Two strong peaks were observed at 619.2 and 630.7 eV (**Figure 4(d)**), which could be assigned to I 3d$_{5/2}$ and I 3d$_{3/2}$, indicating the existence of I$^-$ in the BiOBr$_{1-x}$I$_x$/BiOBr (x = 0.25) samples [26]. Moreover, a minor shift of the Br 3d$_{3/2}$ andBr 3d$_{5/2}$ binding energies was observed for the BiOBr$_{1-x}$I$_x$/BiOBr (x = 0.25) composite, which increased to 69.6 eV and 68.5 eV, respectively. Similarly, the binding energies of I 3d$_{3/2}$ and I 3d$_{5/2}$ for the BiOBr$_{1-x}$I$_x$/BiOBr (x = 0.25) composite were also slightly shifted to 630.9 eV and 619.3 eV, respectively. The slight shift of Br and I peaks in BiOBr$_{1-x}$I$_x$/BiOBr (x = 0.25) is probably due to the interaction

between different halogen atoms [29].

Raman spectroscopy is an appropriate technique for probing the local structure of materials because the bonding states in the coordination polyhedra of a material can be deduced directly from the Raman vibrational spectrum. Raman spectra of the synthesized BiOBr, BiOI and BiOBr$_{1-x}$I$_x$/BiOBr with various Bi/I ratio were recorded to identify the local structure information (Figure 5). Pure BiOBr shows two distinctive bands (110 and 158 cm^{-1}). The A_{1g} internal Bi-Br stretching is probably overlapped by the strong band at 110 cm^{-1}, and the band at 158 cm^{-1} can be ascribed to E_g internal Bi-Br stretching mode [30] [31]. The band at 85 cm^{-1} (assigned to the A_{1g} internal Bi-I stretching mode) and the band at 148 cm^{-1} (assigned to the E_g internal Bi-I stretching mode) of BiOI can be observed [32] [33].

As for the BiOBr$_{1-x}$I$_x$/BiOBr (x = 0.25) composite, the Raman peak assigned to A_{1g} internal Bi-Br stretching shifts to higher wavenumbers, which can be attributed to the fact thatiodine doping might produce intrinsic stresses on the crystal structure in which therefore alter the periodicity of the lattice [30] [34] and result in the distortion of the local structure. The distortion in the local structure leads to overlap between the Bi 6s and the p orbital of halogen. The greater the degree of distortion of the local structure, the more intrinsic stresses on the crystal structurewill be produced, which enhances the migration of photogenerated holes. This result can also be deduced from the results obtained by XRD and XPS.

Figure 6 is the N$_2$ adsorption-desorption isotherms of the photocatalysts, and all samples showed a type IV curve [35]. And the BiOI had the highest surface area of 52.5 m^2/g among all the samples. It may result from the thinner and more unconsolidated structure of BiOI. Generally, there was a positive correlation between the BET surface area and the photocatalytic activity. Simply judging from the surface areas of the as-synthesized samples, the BiOI should have better photocatalytic activity. However, the BiOBr$_{1-x}$I$_x$/BiOBr (x = 0.25) composite has a higher photocatalytic activity. Therefore, it is reasonable to extrapolate
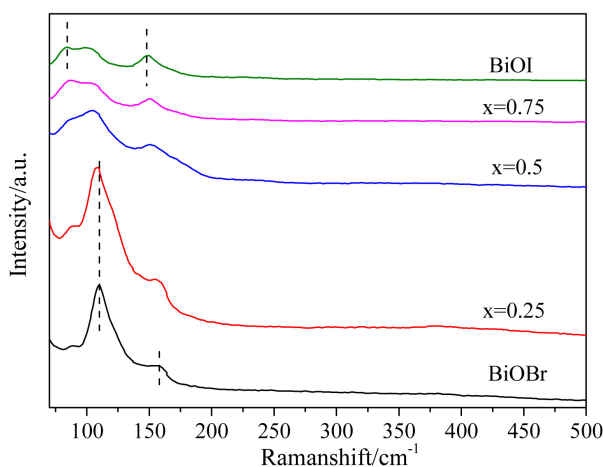

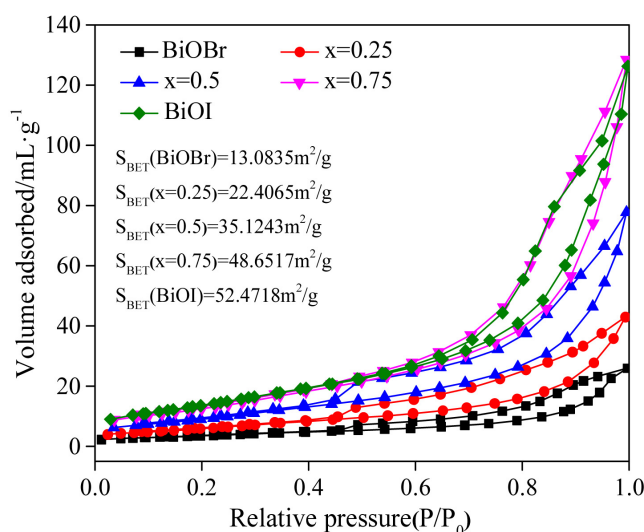**Figure 5.** Raman spectra of the as-prepared samples.

Figure 6. Nitrogen adsorption-desorption isotherms of the as-synthesized samples.

that the S_{BET} value of the samples is a possible factor that may influence the capability of a photocatalyst, but not the only reason in this system.

3.2. Photocatalytic Activity

Phenolphotodegradation was used as a model reaction to evaluate the photoactivities of the as-prepared samples. As depicted in **Figure 7(a)**, without irradiation, it can be observed that the phenol and catalyst suspensions reach absorption-desorption equilibrium at 60 min, and all samples show a small adsorption ability of phenol. Under visible light irradiation, the blank experiment reveals that phenol is barely decomposed without photocatalysts. For the pure BiOBr and BiOI, the concentration of phenol was only reduced by about 40.8% and 63.9% after 150 min of visible-light irradiation. In contrast, the photodegradation activity of as-prepared $BiOBr_{1-x}I_x$/BiOBr (x = 0.25) composite is significantly enhanced, and 92.5% of phenol can be degraded after 150 min irradiation. As shown in insert of **Figure 7(b)**, the pseudo first-order linear relationship is revealed by the plots of $\ln(C/C_0)$ vs irradiation time (t). The apparent reaction rate constant (k) of $BiOBr_{1-x}I_x$/BiOBr (x = 0.25) is calculated as 0.01943 min^{-1}. Moreover, during the photocatalysis characterization of the as-synthesized samples, the concentration of total organic carbon (TOC) was evaluated. The TOC value of phenol was reduced by about 56.4% after 150 min of visible-light irradiation for $BiOBr_{1-x}I_x$/BiOBr (x = 0.25) photocatalysts, which showed the evidence of the decomposition of phenol into carbon dioxide [36].

Furthermore, the recyclability of the $BiOBr_{1-x}I_x$/BiOBr (x = 0.25) composite in the degradation of phenol is considered. After the complete degradation of phenol, the catalyst was collected by centrifugation, and reused in the next cycle. As shown in **Figure 8(a)**, after four cycles of repeated use, a phenol degradation efficiency of 87.6% is still obtained. And no distinct changes in the morphology
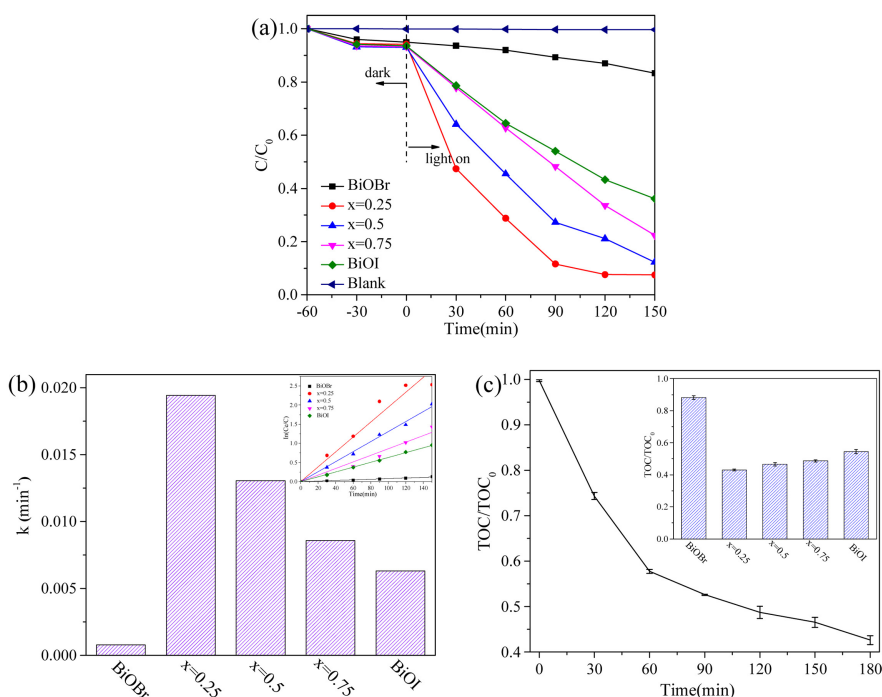
Figure 7. (a) Photocatalytic degradation of phenol under visible light irradiation over different samples; (b) k of the series of as-prepared samples in the degradation of phenol under visible light irradiation and pseudo first order kinetic fitting and the determined apparent rate constants k (insert of Figure (b)); (c) TOC removal of phenol over $BiOBr_{1-x}I_x/BiOBr$ (x = 0.25) composites under visible-light illumination and TOC removal of phenoloveras-synthesized samples (inset of Figure (c)).
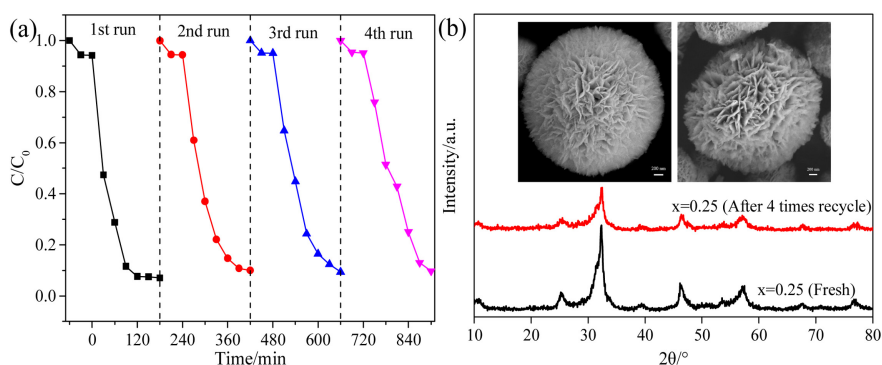

Figure 8. (a) Cycle runs of $BiOBr_{1-x}I_x/BiOBr$ (x = 0.25) composite for degradation of phenol under visible-light irradiation; (b) XRD patterns and (inset of (b)) SEM before and after the cycle runs.

and structure were found for the $BiOBr_{1-x}I_x/BiOBr$ (x = 0.25) photocatalyst after 4 runs of cycling experience, as shown in XRD patterns (**Figure 8(b)**), which indicates the structure of the photocatalyst is extremely stable and has not been significantly changed during the reaction process. **Figure 8(c)** exhibits the SEM of $BiOBr_{1-x}I_x/BiOBr$ (x = 0.25) composite before and after 4runs cycling reaction. It can be seen that the composite still keeps a good hierarchical microsphere-shape.

Moreover, other persistence organic contaminants, such as BPA and 2,4-DCP, can also be degraded efficiently, verifying the common applicability of $BiOBr_{1-x}I_x/BiOBr$ (x = 0.25) as effective visible-light photocatalyst using in the decomposition of organic compound (**Figure 9**). The total organic carbon (TOC) results show that more than 66% and 44% TOC in the BPA and 2,4-DCP solution are removed within 180 min of irradiation, respectively. All these results confirm the high mineralization activity of $BiOBr_{1-x}I_x/BiOBr$ (x = 0.25) under visible-light irradiation.

3.3. Dependence of Photocatalytic Activity on the Structure

UV-Vis DRS was employed to investigate the photophysical properties of the as-synthesized samples (**Figure 10(a)**). It can be found that all samples show a strong absorption in the visible light region. Compared with BiOBr, with the introduction of iodine into the crystalline BiOBr, the absorption edge of $BiOBr_{1-x}I_x/BiOBr$ samples exhibited red-shift, but band edge shift is still smaller than that of BiOI. This observation suggests that the formation of $BiOBr_{1-x}I_x/BiOBr$ composites can indeed modulate the capacity of visible light absorption to some extent [28]. The band gap energies (E_g) of all samples were obtained by the following formula [37]:

$$\alpha h\upsilon = A\left(h\upsilon - E_g\right)^{\frac{n}{2}} \qquad (1)$$

where α, h, ν and A represent the absorption coefficient, Planck constant and light frequency and proportionality, respectively. And the fundamental absorption of both BiOBr and BiOI are indirect transition between bands, so n is equal to 4.

As shown in **Figure 10(b)**, the band gaps of BiOBr, $BiOBr_{1-x}I_x/BiOBr$ (x = 0.25) and BiOI are 2.66, 2.37 and 1.93 eV, respectively. After the introduction of

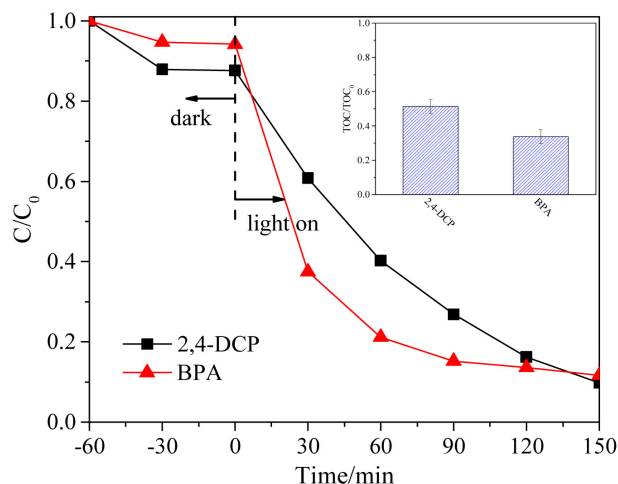**Figure 9.** Photocatalytic degradation of BPA and 2,4-DCP under visible light irradiation over $BiOBr_{1-x}I_x/BiOBr$ (x = 0.25) composite and the reduction in TOC for the degradation of BPA and 2,4-DCP (insideillustration).
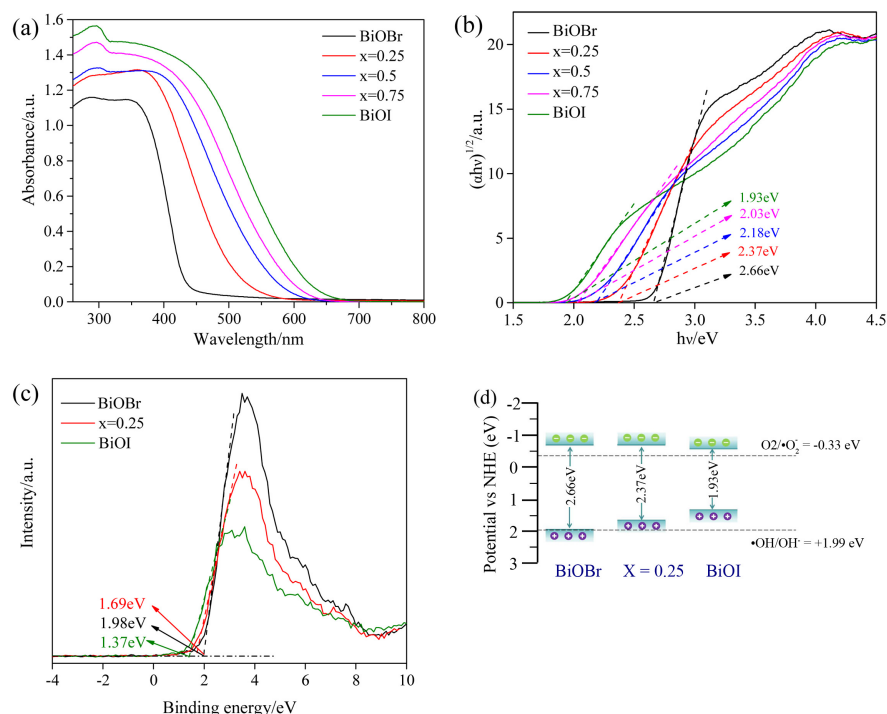
Figure 10. (a) UV-vis diffuse reflection spectra; (b) The bandgap value, estimated by a related curve of $(ah\nu)^{1/2}$ versus photon energy plotted; (c) VB-XPS spectra of BiOBr, BiOBr$_{1-x}$I$_x$/BiOBr (x = 0.25) and BiOI; (d) The band position schematic of BiOBr, BiOBr$_{1-x}$I$_x$/BiOBr (x = 0.25) and BiOI.

iodine ions into the BiOBrlattice, localized levels in the forbidden energy gap were formed, leading to a decrease in the band gap energy [38]. Further, the valence band X-ray photoelectron spectra (VB-XPS) suggested that the positions of valence band of BiOBr, BiOBr$_{1-x}$I$_x$/BiOBr (x = 0.25) and BiOI were 1.98, 1.69 and 1.37 eV, respectively (**Figure 10(c)**). Based on the equation of $E_{CB} = E_g - E_{VB}$ [37], the conduction band (CB) edges of BiOBr, BiOBr$_{1-x}$I$_x$/BiOBr (x = 0.25) and BiOI were calculated to be −0.68, −0.68 and −0.56 eV, respectively. According to the above analysis, the band position schematic of BiOBr, BiOBr$_{1-x}$I$_x$/BiOBr (x = 0.25) and BiOI was obtained, with the results shown in **Figure 10(d)**. The Bi-OBr$_{1-x}$I$_x$/BiOBr (x = 0.25) has a narrower E_g than that of BiOBr, demonstrating that BiOBr$_{1-x}$I$_x$/BiOBr (x = 0.25) is conducive to improve the visible-light absorptive capacity [39]. And the valence band edge of BiOBr$_{1-x}$I$_x$/BiOBr (x = 0.25) is higher than that of BiOI simultaneously, unveiling that BiOBr$_{1-x}$I$_x$/BiOBr (x = 0.25) possesses elevated oxidizing ability [40].

To explore the primary active species generated in the reaction system, trapping experiments of active species were conducted as shown in **Figure 11(a)**. Sodium oxalate (SO), N_2 and isopropanol (IPA) were used as the quenchers for h$^+$, •O_2^- and •OH, respectively. The addition of SO or bubbling N_2 caused the degradation efficiency of phenol decreased to 32.3% and 37.5%. After IPA was added, the photocatalytic efficiency was almost invariable. ESR measurements were employed to evaluate the main oxidative species during the photodegradation
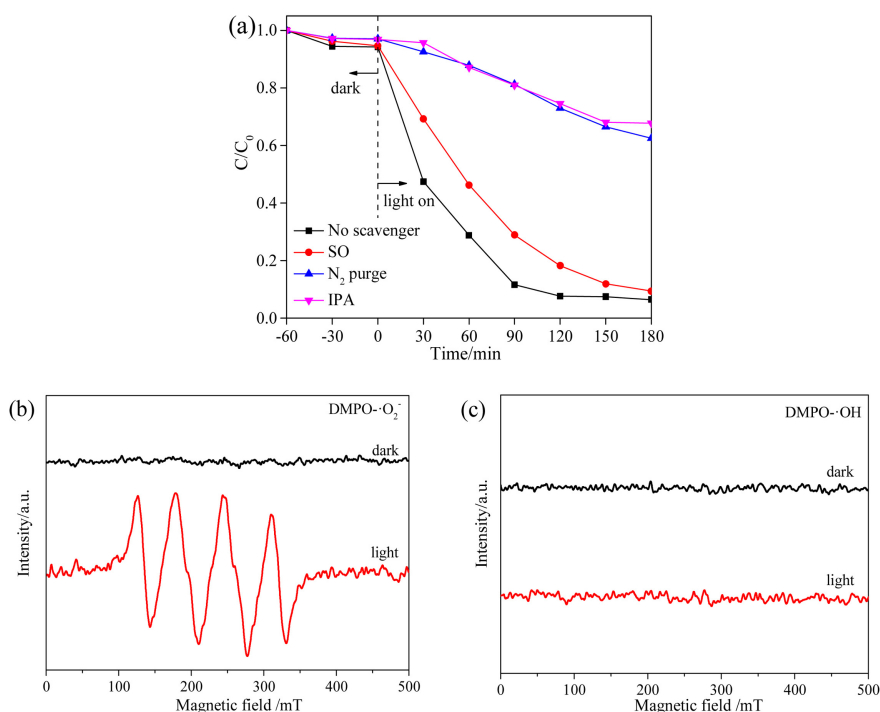
Figure 11. (a) Photocatalytic degradation of phenol over BiOBr$_{1-x}$I$_x$/BiOBr (x = 0.25) under visible light irradiation with different scavengers; (b)The ESR spectra of DMPO- •O$_2^-$ and (c) DMPO- •OH in the presence of BiOBr$_{1-x}$I$_x$/BiOBr (x = 0.25) under dark and visible light irradiation.

process [41]. As shown in **Figure 11(b)** and **Figure 11(c)**, ESR signals of DMPO- •O$_2^-$ adduct and DMPO-•OH adduct are not detected indark. However, strong DMPO- •O$_2^-$ signals were observed after the same irradiated by visible-light, confirming that the photogenerated electrons (e$^-$) on the CB of BiOBr$_{1-x}$I$_x$/BiOBr (x = 0.25) could be trapped to produce •O$_2^-$ [42]. And the characteristic peak of DMPO-•OH cannot be obviously detected under the identical conditions, which is consistent with the scavenger experiments. These indicated that h$^+$ and •O$_2^-$ were significant active species in the photocatalytic process of BiOBr$_{1-x}$I$_x$/BiOBr (x = 0.25), while •OH was not the major reactive species.

To investigate the transportation behaviors of the photoexcited charges in these samples, the photoelectrochemical analyses were carried out. **Figure 12(a)** records the transient photocurrent responses of the catalysts under visible light irradiation. Among all of the samples, BiOBr$_{1-x}$I$_x$/BiOBr (x = 0.25) shows the most intensity signal of photocurrent density. This result revealed that less recombination and longer lifetime of photoinduced charges than those of others, which unveils that charge separation efficiency can be enhanced by the internal electric fields and band match [43]. Further, **Figure 12(b)** shows the the electrochemical impedance spectra (EIS) of the samples. Normally, the smaller radius in an EIS Nyquist is, the better charge transfer ability would be, which would impede the recombination of photogenerated charge carriers [44]. The BiOBr$_{1-x}$I$_x$/BiOBr (x = 0.25) composite has the smallest radius with respect to
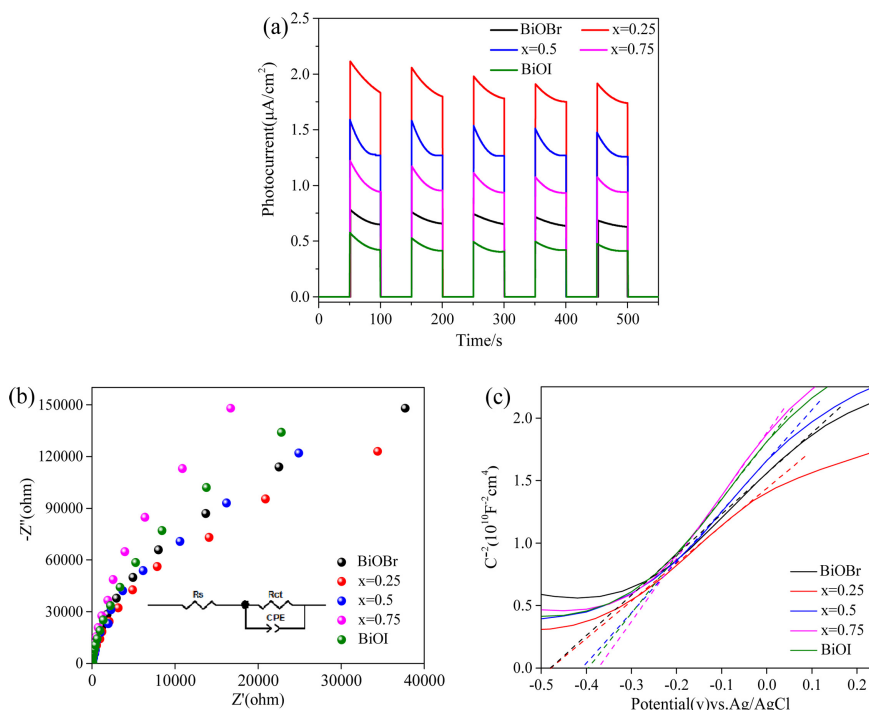
Figure 12. (a) Transient photocurrent responses; (b) electrochemical impedance spectra of the samples under visible light irradiation; (c) Mott-Schottky plots for the as-synthesized samples.

other samples, indicating much lower electron transfer resistance than that of the other samples, and therefore, defines higher charge transfer efficiency [43] [45]. As shown in **Figure 12(c)**, all samples are regarded as n-type semiconductors because of the positive slope of the Mott-Schottky curve [46]. If the slope in a Mott-Schottky plot is lower, the carrier concentration is higher [47] [48]. It is indicated that the $BiOBr_{1-x}I_x/BiOBr$ (x = 0.25) composite has the highest carrier concentration. Accordingly, the enhancement of separation efficiency of photoinduced electron-hole pairs (e^--h^+) ought to be another origin of excellent photoactivity of $BiOBr_{1-x}I_x/BiOBr$ (x = 0.25).

The enhanced photocatalytic activity of $BiOBr_{1-x}I_x/BiOBr$ (x = 0.25) originated from the fast separation of photo generated charges under visible light. On the basis of the above results and previous reports [15] [46], a possible mechanism for the enhanced photocatalytic activity over the $BiOBr_{1-x}I_x/BiOBr$ (x = 0.25) is shown schematically in **Figure 13**. On the one hand, since the iodine element has the optimum size and valence, with the introduction of iodine into the crystalline BiOBr, the local tension around the iodine in the crystal lattice changes, resulting in a change in the delocalization energy. And so on, the IEF increases [49]. The IEF drives e^- and h^+ move from the separation sites to [Bi_2O_2] and [Br] slices [9]. Therefore, the charge recombination was drastically inhibited, which was of great benefit for enhancing the photocatalytic activity [36] (**Figure 13(a)**). On the other hand, as shown in **Figure 13(b)**, under visible light, both$BiOBr_{1-x}I_x$ and BiOBr can be simultaneously excited, the photoexcited electrons transferred
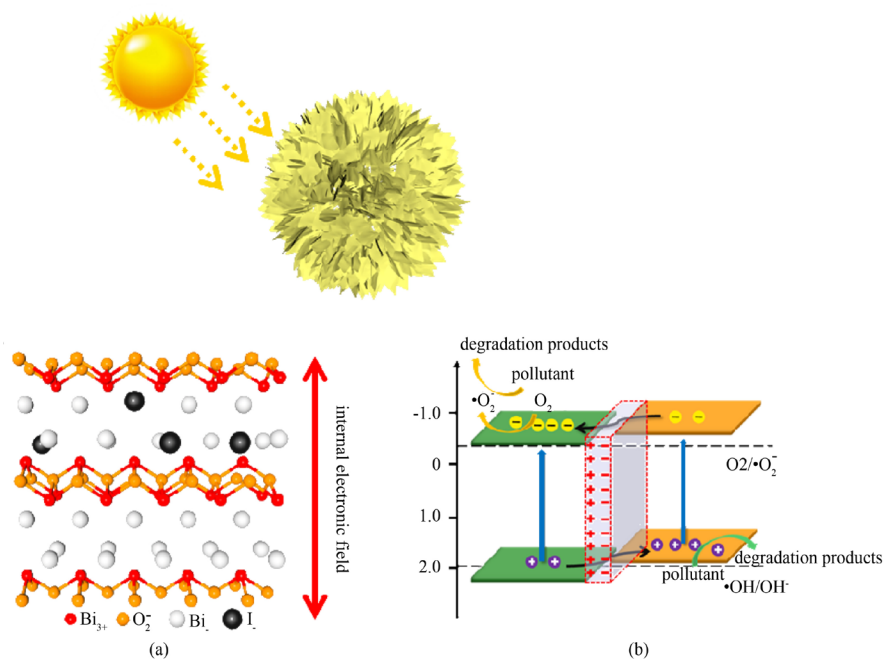
Figure 13. Schematic illustration of electron-hole separation and transport in the BiOBr$_{1-x}$I$_x$/BiOBr composites photocatalyst.

from CB of the BiOBr$_{1-x}$I$_x$ to that of BiOBr, and since the VB of BiOBr (1.98 eV) was more positive than that of BiOBr$_{1-x}$I$_x$ (1.69 eV), the photoexcited holes on BiOBr could transfer to the VB of BiOBr$_{1-x}$I$_x$ driven by CB offset of 0.29 eV. The potential difference was the main driving force for efficient charge separation and transfer [50]. As the photogenerated electrons and holes were spatially separated into two different components, the charge recombination was drastically inhibited, which was of great benefit for enhancing the photocatalytic activity [51]. Because the redox potential of O$_2$/•O$_2^-$ was −0.33 V vs. NHE at pH about 7 [52], the electrons assembled on the conduction band of BiOBr had enough driving force (−0.68 V) to react with O$_2$ to form •O$_2^-$ reactive species for degrading pollutants. At the same time, the photoinduced holes gathered at the valence band of BiOBr$_{1-x}$I$_x$ directly oxidize pollutants to the final degradation products. Therefore, BiOBr$_{1-x}$I$_x$/BiOBr (x = 0.25) exhibits the improved photocatalytic activity by the synergistic effect of IEF and heterojunction, which could be utilized as the manipulating strategy for high effective catalyst.

4. Conclusion

Based on the above systematic investigations, BiOBr$_{1-x}$I$_x$/BiOBr photocatalyst exhibiting the three-dimensional hierarchical microsphere structure were successfully constructed through a facile solvothermal method. BiOBr$_{1-x}$I$_x$/BiOBr (x = 0.25) sample exhibited the highest photocatalytic activity, which showed a reaction rate constant as high as 0.01943 min^{-1}, 24.56 and 3.08 times higher than that of pure BiOBr and BiOI for the photodegradation of phenol, respectively. It possessed good stability and durability, favoring long-time use. The synergistic

effect between IEF and heterojunction construction, which resulted by the local structure distortion provided the efficient charge separation. This work is useful to provide a new different insight into the environmental remediation.

Acknowledgements

Conflicts of Interest

The authors declare no conflicts of interest regarding the publication of this paper.

References

[1] Ji, F., Li, C.L. and Zhang, J.H. (2010) Hydrothermal Synthesis of $Li_9Fe_3(P_2O_7)_3(PO_4)_2$ Nanoparticles and Their Photocatalytic Properties under Visible-Light Illumination. *ACS Applied Materials & Interfaces*, **2**, 1674-1678. https://doi.org/10.1021/am100189m

[2] Pan, Y.X., You, Y., Xin, S., Li, Y.T., Fu, G.T. and Cui, Z.M. (2017) Goodenough, Photocatalytic CO_2 Reduction by Carbon-Coated Indium-Oxide Nanobelts. *Journal of the American Chemical Society*, **139**, 4123-4129. https://doi.org/10.1021/jacs.7b00266

[3] Schneider, J., Matsuoka, M., Takeuchi, M., Zhang, J.L., Yu, H., Masakazu, A. and Detlef, W.B. (2014) Understanding TiO_2 Photocatalysis: Mechanisms and Materials. *Chemical Reviews*, **114**, 9919-9986. https://doi.org/10.1021/cr5001892

[4] Bai, S., Jiang, W.Y., Li, Z.Q. and Xiong, Y.J. (2015) Surface and Interface Engineering in Photocatalysis. *ChemNanoMat*, **1**, 223-239. https://doi.org/10.1002/cnma.201500069

[5] Yang, J.H., Wang, D., Han, H.X. and Li, C. (2013) Roles of Cocatalysts in Photocatalysis and Photoelectrocatalysis. *Accounts of Chemical Research*, **46**, 1900-1909. https://doi.org/10.1021/ar300227e

[6] Lou, Z.Z., Wang, P., Huang, B.B., Dai, Y., Qin, X.Y., Zhang, X.Y., Wang, Z.Y. and Liu, Y.Y. (2017) Enhancing Charge Separation in Photocatalysts with Internal Polar Electric Fields. *ChemPhotoChem*, **1**, 136-147. https://doi.org/10.1002/cptc.201600057

[7] Sun, L.M., Xiang, L., Zhao, X., Jia, C.J., Yang, J., Jin, Z., Cheng, X.F. and Fan, W.L. (2015) Enhanced Visible-Light Photocatalytic Activity of BiOI/BiOCl Heterojunctions: Key Role of Crystal Facet Combination. *ACS Catalysis*, **5**, 3540-3551. https://doi.org/10.1021/cs501631n

[8] Cao, T.P., Li, Y.J., Wang, C.H., Shao, C.L. and Liu, Y.C. (2011) A Facile in Situ Hydrothermal Method to $SrTiO_3/TiO_2$ Nanofiber Heterostructures with High Photocatalytic Activity. *Langmuir*, **27**, 2946-2952. https://doi.org/10.1021/la104195v

[9] Li, J., Cai, L.J., Shang, J., Yu, Y. and Zhang, L.Z. (2016) Giant Enhancement of Internal Electric Field Boosting Bulk Charge Separation for Photocatalysis. *Advanced*

Materials, **28**, 4059-4064. https://doi.org/10.1002/adma.201600301

[10] Ren, X.J., Li, J.B., Cao, X.Z., Wang, B.Y., Zhang, Y.F. and Wei, Y. (2019) Synergistic Effect of Internal Electric Field and Oxygen Vacancy on Thephotocatalytic Activity of $BiOBr_xI_{1-x}$ with Isomorphous Fluorine Substitution. *Journal of Colloid and Interface Science*, **554**, 500-511. https://doi.org/10.1016/j.jcis.2019.07.034

[11] Hu, T.P., Yang, Y., Dai, K., Zhang, J.F. and Liang, C.H. (2018) A Novel Z-Scheme Bi_2MoO_6/BiOBr Photocatalyst for Enhanced Photocatalytic Activity under Visible Light Irradiation. *Applied Surface Science*, **456**, 473-481. https://doi.org/10.1016/j.apsusc.2018.06.186

[12] Xiang, Y.H., Ju, P., Wang, Y., Sun, Y., Zhang, D. and Yu, J.Q. (2016) Chemical Etching Preparation of the Bi_2WO_6/BiOI p-n Heterojunction with Enhanced Photocatalytic Antifouling Activity under Visible Light Irradiation. *Chemical Engineering Journal*, **288**, 264-275. https://doi.org/10.1016/j.cej.2015.11.103

[13] Su, Y., Zhang, L. and Wang, W.Z. (2016) Internal Polar Field Enhanced H_2 Evolution of $BiOIO_3$ Nanoplates. *International Journal of Hydrogen Energy*, **41**, 10170-10177. https://doi.org/10.1016/j.ijhydene.2016.04.236

[14] Huang, H.W., He, Y., Li, X.W., Li, M., Zeng, C., Dong, F., Du, X., Zhang, T.R. and Zhang, Y.H. (2015) $Bi_2O_2(OH)(NO_3)$ as a Desirable $[Bi_2O_2]^{2+}$ Layered Photocatalyst: Strong Intrinsic Polarity, Rational Band Structure and {001} Active Facets Co-Beneficial for Robust Photooxidation Capability. *Journal of Materials Chemistry A*, **3**, 24547-24556. https://doi.org/10.1039/C5TA07655B

[15] Li, X., Chen, T.D., Lin, H.L., Cao, J., Huang, H.W. and Chen, S.F. (2018) Intensive Photocatalytic Activity Enhancement of Bi_5O_7I via Coupling with Band Structure and Content Adjustable $BiOBr_xI_{1-x}$. *Science Bulletin*, **63**, 219-227. https://doi.org/10.1016/j.scib.2017.12.016

[16] Hao, L., Huang, H.W., Guo, Y.X. and Zhang, Y.H. (2018) Multi-Functional $Bi_2O_2(OH)(NO_3)$ Nanosheets with {001} Active Exposing Facets: Efficient Photocatalysis, Dye-Sensitization and Piezoelectric-Catalysis. *ACS Sustainable Chemistry & Engineering*, **6**, 1848-1862. https://doi.org/10.1021/acssuschemeng.7b03223

[17] Jiang, J., Zhao, K., Xiao, X.Y. and Zhang, L.Z. (2012) Synthesis and Facet-Dependent Photoreactivity of BiOCl Single Crystalline Nanosheets. *Journal of the American Chemical Society*, **134**, 4473-4476. https://doi.org/10.1021/ja210484t

[18] Wang, L., Min, X.P., Sui, X.Y., Chen, J.H. and Wang, Y. (2020) Facile Construction of Novel $BiOBr/Bi_{12}O_{17}Cl_2$ Heterojunction Composites with Enhanced Photocatalytic Performance. *Journal of Colloid and Interface Science*, **560**, 21-33. https://doi.org/10.1016/j.jcis.2019.10.048

[19] Wu, D., Wang, B., Wang, W., An, T.C., Li, G.Y., Ng, T.W., Ho Y.Y., Xiong, C.M., Hung, K.L. and Wong, P.K. (2015) Visible-Light-Driven BiOBr Nanosheets for Highly Facet-Dependent Photocatalytic Inactivation of *Escherichia coli*. *Journal of Materials Chemistry A*, **3**, 15148-15155. https://doi.org/10.1039/C5TA02757H

[20] Liu, Q.Y., Han, G., Zheng, Y.F. and Song, X.C. (2018) Synthesis of $BiOBr_xI_{1-x}$ Solid Solutions with Dominant Exposed {001} and {110} Facets and Their Visible-Light-Induced Photocatalytic Properties. *Separation and Purification Technology*, **203**, 75-83. https://doi.org/10.1016/j.seppur.2018.04.011

[21] Zhang, X., Wang, C.Y., Wang, L.W., Huang, G.X., Wang, W.K. and Yu, H.Q. (2016) Fabrication of $BiOBr_xI_{1-x}$ Photocatalysts with Tunable Visible Light Catalytic Activity by Modulating Band Structures. *Scientific Reports*, **6**, Article No. 22800. https://doi.org/10.1038/srep22800

[22] Gao, S.W., Guo, C.S., Hou, S., Wan, L., Wang, Q., Lv, J.P., Zhang, Y., Gao, J.F.,

Meng, W. and Xu, J. (2017) Photocatalytic Removal of Tetrabromobisphenol A by Magnetically Separable Flower-Like BiOBr/BiOI/Fe$_3$O$_4$ Hybrid Nanocomposites under Visible-Light Irradiation. *Journal of Hazardous Materials*, **331**, 1-12.
https://doi.org/10.1016/j.jhazmat.2017.02.030

[23] Bai, Y., Shi, X., Wang, P.Q., Wang, L., Zhang, K., Zhou, Y., Xie, H.Q., Wang, J. and Ye, L.Q. (2019) BiOBr$_x$I$_{1-x}$/BiOBr Heterostructure Engineering for Efficient Molecular Oxygen Activation. *Chemical Engineering Journal*, **356**, 34-42.
https://doi.org/10.1016/j.cej.2018.09.006

[24] Jia, Z., Wang, F., Xin, F. and Zhang, B. (2011) Simple Solvothermal Routes to Synthesize 3D BiOBr$_x$I$_{1-x}$ Microspheres and Their Visible-Light-Induced Photocatalytic Properties. *Industrial and Engineering Chemistry Research*, **50**, 6688-6694.
https://doi.org/10.1021/ie102310a

[25] Hao, Q., Wang, R.T., Lu, H.J., Xie, C.A., Ao, W.H., Chen, D.M., Ma, C., Yao, W.Q. and Zhu, Y.F. (2017) One-Pot Synthesis of C/Bi/Bi$_2$O$_3$ Composite with Enhanced Photocatalytic Activity. *Applied Catalysis B: Environmental*, **219**, 63-72.
https://doi.org/10.1016/j.apcatb.2017.07.030

[26] Zhang, X., Wang, C.Y., Wang, L.W., Huang, G.X., Wang, W.K. and Yu, H.Q. (2016) Fabrication of BiOBr$_x$I$_{1-x}$ Photocatalysts with Tunable Visible Light Catalytic Activity by Modulating Band Structures. *Scientific Reports*, **6**, Article No. 22800.
https://doi.org/10.1038/srep22800

[27] Di, J., Xia, J.X., Ji, M.X., Yin, S., Li, H.P., Xu, H., Zhang, Q. and Li, H.M. (2015) Controllable Synthesis of Bi$_4$O$_5$Br$_2$ Ultrathin Nanosheets for Photocatalytic Removal of Ciprofloxacin and Mechanism Insight. *Journal of Materials Chemistry A*, **3**, 15108-15118. https://doi.org/10.1039/C5TA02388B

[28] Bai, Y., Ye, L.Q., Chen, T., Wang, P.Q., Wang, L., Shi, X. and Wong P.K. (2017) Synthesis of Hierarchical Bismuth-Rich Bi$_4$O$_5$BrxI$_{2-x}$ Solid Solutions for Enhanced Photocatalytic Activities of CO$_2$ Conversion and Cr(VI) Reduction under Visible Light. *Applied Catalysis B: Environmental*, **203**, 633-640.
https://doi.org/10.1016/j.apcatb.2016.10.066

[29] Kong, L., Jiang, Z., Lai, H.H., Nicholls, R.J., Xiao, T.C., Jones, M.O. and Edwards, P.P. (2012) Unusual Reactivity of Visible-Light-Responsive AgBr-BiOBr Heterojunction Photocatalysts, *Journal of Catalysis*, **293**, 116-125.
https://doi.org/10.1016/j.jcat.2012.06.011

[30] Cai, L., Zhang, G.Q., Zhang, Y.F. and Wei, Y. (2018) Mediation of Band Structure for BiOBr$_x$I$_{1-x}$ Hierarchical Microsphere of Multiple Defects with Enhanced Visible-Light Photocatalytic Activity. *CrystEngComm*, **20**, 3647-3656.
https://doi.org/10.1039/C8CE00700D

[31] Zhang, D., Li, J., Wang, Q.Q. and Wu, Q.S. (2013) High {001} Facets Dominated BiOBr Lamellas: Facile Hydrolysis Preparation and Selective Visible-Light Photocatalytic Activity. *Journal of Materials Chemistry A*, **1**, 8622.
https://doi.org/10.1039/c3ta11390f

[32] Huang, Y., Li, H., Fan, W., Zhao, F., Qiu, W., Ji, H. and Tong, Y. (2016) Defect Engineering of Bismuth Oxyiodide by IO$_3$ Doping for Increasing Charge Transport in Photocatalysis, *ACS Applied Materials & Interfaces*, **8**, 27859-27867.
https://doi.org/10.1021/acsami.6b10653

[33] Cao, J., Xu, B.Y., Lin, H.L., Luo, B.D. and Chen, S.F. (2012) Novel Heterostructured Bi$_2$S$_3$/BiOI Photocatalyst: Facile Preparation, Characterization and Visible Light Photocatalytic Performance. *Dalton Transactions*, **41**, 11482-11490.
https://doi.org/10.1039/c2dt30883e

[34] Liu, X.Y, Su, Y.G., Zhao, Q.H., Du, C.F. and Liu, Z.L. (2016) Constructing $Bi_{24}O_{31}Cl_{10}$/BiOCl Heterojunction via a Simple Thermal Annealing Route for Achieving Enhanced Photocatalytic Activity and Selectivity. *Scientific Reports*, **6**, Article No. 28689. https://doi.org/10.1038/srep28689

[35] Chen, W., Liu, T.Y., Huang, T., Liu, X.H. and Yang, X.J. (2016) Novel Mesoporous P-Doped Graphitic Carbon Nitride Nanosheets Coupled with $ZnIn_2S_4$ Nanosheets as Efficient Visible Light Driven Heterostructures with Remarkably Enhanced Photo-Reduction Activity. *Nanoscale*, **8**, 3711-3719. https://doi.org/10.1039/C5NR07695A

[36] Yang, X.L., Qian, F.F., Wang, Y., Li, M.L., Lu, J.R., Li, Y.M. and Bao, M.T. (2017) Constructing a Novel Ternary Composite $(C_{16}H_{33}(CH_3)_3N)_4W_{10}O_{32}$/g-$C_3N_4$/rGO with Enhanced Visible-Light-Driven Photocatalytic Activity for Degradation of Dyes and Phenol. *Applied Catalysis B: Environmental*, **200**, 283-296. https://doi.org/10.1016/j.apcatb.2016.07.024

[37] Wang, Q., Wang, W., Zhong, L.L., Liu, D.M., Cao, X.Z. and Cui, F.Y. (2018) Oxygen Vacancy-Rich 2D/2D BiOCl-g-C_3N_4 Ultrathin Heterostructure Nanosheets for Enhanced Visible-Light-Driven Photocatalytic Activity in Environmental Remediation. *Applied Catalysis B: Environmental*, **220**, 290-302. https://doi.org/10.1016/j.apcatb.2017.08.049

[38] Cho, E.C., Chang-Jian, C.W., Huang, J.H., Lee, G.Y., Hung, W.H., Sung, M.Y., Lee, K.C., Weng, H.C., Syu, W.L., Hsiaog, Y.S. and Chen, C.P. (2021) Co^{2+}-Doped BiOBr$_x$Cl$_{1-x}$ Hierarchical Microspheres Display Enhanced Visible-Light Photocatalytic Performance in the Degradation of Rhodamine B and Antibiotics and the Inactivation of *E. coli*. *Journal of Hazardous Materials*, **402**, 12345. https://doi.org/10.1016/j.jhazmat.2020.123457

[39] Xu, H.Y., Han, X., Tan, Q., He, X.L. and Qi, S.Y. (2017) Structure-Dependent Photocatalytic Performance of BiOBr$_x$I$_{1-x}$ Nanoplate Solid Solutions. *Catalysts*, **7**, 153. https://doi.org/10.3390/catal7050153

[40] Xia, P.F., Zhu, B.C., Yu, J.G., Cao, S.W. and Jaroniec, M. (2017) Ultra-Thin Nanosheet Assemblies of Graphitic Carbon Nitride for Enhanced Photocatalytic CO_2 Reduction. *Journal of Materials Chemistry A*, **5**, 3230-3238. https://doi.org/10.1039/C6TA08310B

[41] Hong, Y.Z., Jiang, Y.H., Li, C.S., Fan, W.Q., Yan, X., Yan, M. and Shi, W.D. (2016) *In-Situ* Synthesis of Direct Solid-State Z-Scheme V_2O_5/g-C_3N_4 Heterojunctions with Enhanced Visible Light Efficiency in Photocatalytic Degradation of Pollutant. *Applied Catalysis B: Environmental*, **180**, 663-673. https://doi.org/10.1016/j.apcatb.2015.06.057

[42] Mao, D.J., Ding, S.S., Meng, L.J., Dai, Y.X., Sun, C., Yang, S.G. and He, H. (2017) One-Pot Microemulsion-Mediated Synthesis of Bi-Rich $Bi_4O_5Br_2$ with Controllable Morphologies and Excellent Visible-Light Photocatalytic Removal of Pollutants. *Applied Catalysis B: Environmental*, **207**, 153-165. https://doi.org/10.1016/j.apcatb.2017.02.010

[43] Zhang, D., Guo, Y.L. and Zhao, Z.K. (2018) Porous Defect-Modified Graphitic Carbon Nitride via a Facile One-Step Approach with Significantly Enhanced Photocatalytic Hydrogen Evolution under Visible Light Irradiation. *Applied Catalysis B: Environmental*, **226**, 1-9. https://doi.org/10.1016/j.apcatb.2017.12.044

[44] Hou, Y., Zuo, F., Dagg, A. and Feng, P.Y. (2012) Visible Light-Driven α-Fe_2O_3 Nanorod/Graphene/BiV$_{1-x}$Mo$_x$O$_4$ Core/Shell Heterojunction Array for Efficient Photoelectrochemical Water Splitting. *Nano Letter*, **12**, 6464-6473. https://doi.org/10.1021/nl303961c

[45] Wang, W., You, S.J., Gong, X.B., Qi, D.P., Chandran, B.K., Bi, L.P., Cui, F.Y. and Chen, X.D. (2016) Bioinspired Nanosucker Array for Enhancing Bioelectricity Generation in Microbial Fuel Cells. *Advanced Materials*, **28**, 270-275. https://doi.org/10.1002/adma.201503609

[46] Zeng, C., Hu, Y.M. and Huang, H.W. (2017) $BiOBr_{0.75}I_{0.25}/BiOIO_3$ as a Novel Heterojunctional Photocatalyst with Superior Visible-Light-Driven Photocatalytic Activity in Removing Diverse Industrial Pollutants. *ACS Sustainable Chemistry & Engineering*, **5**, 3897-3905. https://doi.org/10.1021/acssuschemeng.6b03066

[47] Luo, W.J., Yang, Z.S., Li, Z.S., Zhang, J.Y., Liu, J.G., Zhao, Z.Y., Wang, Z.Q., Yan, S.C., Yu, T. and Zou, Z.G. (2011) Solar Hydrogen Generation from Seawater with a Modified $BiVO_4$ Photoanode. *Energy & Environmental Science*, **4**, 4046-4051. https://doi.org/10.1039/c1ee01812d

[48] Luo, W.J., Wang, J.J., Zhao, X., Zhao, Z.Y., Li, Z.S. and Zou, Z.G. (2013) Formation Energy and Photoelectrochemical Properties of $BiVO_4$ after Doping at Bi^{3+} or V^{5+} Sites with Higher Valence Metal Ions. *Physical Chemistry Chemical Physics*, **15**, 1006-1013. https://doi.org/10.1039/C2CP43408C

[49] Chen, F., Huang, H.W., Guo, L., Zhang, Y.H. and Ma, T.Y. (2019) The Role of Polarization in Photocatalysis. *Angewandte Chemie*, **58**, 10061-10073. https://doi.org/10.1002/anie.201901361

[50] Zhang, S.W., Li, J.X., Wang, X.K., Huang, Y.S., Zeng, M.Y. and Xu, J.Z. (2015) Rationally Designed 1D $Ag@AgVO_3$ Nanowire/Graphene/Protonated $g-C_3N_4$ Nanosheet Heterojunctions for Enhanced Photocatalysis via Electrostatic Self-Assembly and Photochemical Reduction Methods. *Journal of Materials Chemistry A*, **3**, 10119-10126. https://doi.org/10.1039/C5TA00635J

[51] Zhou, X.F., Yan, F., Wu, S.H., Shen, B., Zeng, H.R. and Zhai, J.W. (2020) Remarkable Piezophoto Coupling Catalysis Behavior of $BiOX/BaTiO_3$ (X = Cl, Br, $Cl_{0.166}Br_{0.834}$) Piezoelectric Composites. *Small*, **16**, Article ID: 2001573. https://doi.org/10.1002/smll.202001573

[52] Li, Z.H., Dong, T.T., Zhang, Y.F., Wu, L., Li, J.Q., Wang, X.X. and Fu, X.Z. (2007) Studies on $In(OH)_yS_z$ Solid Solutions: Syntheses, Characterizations, Electronic Structure, and Visible-Light-Driven Photocatalytic Activities. *The Journal of Physical Chemistry C*, **111**, 4727-4733. https://doi.org/10.1021/jp066671m